frontiers | Frontiers in Mechanical Engineering

TYPE Original Research
PUBLISHED 04 December 2025
DOI 10.3389/fmech.2025.1729318

OPEN ACCESS

EDITED BY
Fen Lin,
Nanjing University of Aeronautics and Astronautics, China

REVIEWED BY
Guifu Du,
Soochow University, China
Yong Wang,
Jiangsu University, China

*CORRESPONDENCE
Ronglin Yan,
Y00450240442@njit.edu.cn

RECEIVED 21 October 2025
REVISED 28 October 2025
ACCEPTED 03 November 2025
PUBLISHED 04 December 2025

CITATION
Zhang Y, Yan R and Yang W (2025) Inertially-enhanced damping energy sink for synergistic vibration-lightweight optimization in half-car suspensions.
Front. Mech. Eng. 11:1729318.
doi: 10.3389/fmech.2025.1729318

Inertially-enhanced damping energy sink for synergistic vibration-lightweight optimization in half-car suspensions

Yuanyuan Zhang, Ronglin Yan* and Weifeng Yang

School of Transportation Engineering, Nanjing Institute of Technology, Nanjing, China

When applying Nonlinear Energy Sinks (NES) to vehicle suspension systems, these systems exhibit frequency sensitivity, and effective vibration reduction typically requires a relatively large mass. To address these limitations, this paper proposes an Inertially-Enhanced Damping Energy Sink (IDES). The study begins by establishing a single-degree-of-freedom vibration model to investigate the optimal configuration of the IDES. Subsequently, the effective IDES structure is applied to a half-vehicle model, and its dynamic response is solved using the Harmonic Balance Method (HBM) and the Pseudo-Arc Length Method (PALM). Under both harmonic and random excitations, the results demonstrate that the IDES significantly suppresses the resonance peak and reduces the vehicle's vertical acceleration, as well as the dynamic deflections of the front and rear suspensions and the dynamic loads on the front and rear tires. To optimize the vehicle's vertical and pitch angular accelerations, a genetic algorithm was employed to determine the optimal structural parameters of the IDES within the half-vehicle system. The results indicate that, compared to the NES system, the vibration reduction system with optimized IDES parameters reduces the RMS values of the vertical body acceleration by 5.56%, the front and rear suspension dynamic deflections by 9.20% and 15.56%, and the front and rear tire dynamic loads by 11.37% and 12.15%, respectively, while maintaining the pitch angular acceleration within an allowable range. Leveraging nonlinear damping and inertial mass amplification, the IDES structure overcomes the traditional NES's dependence on cubic stiffness, offering advantages in both wide-band vibration reduction and lightweight design for vehicle suspension systems. The optimization of IDES parameters using a genetic algorithm further enhances the performance of this new damping structure. The proposed IDES structure and optimization strategy can serve as a valuable reference for the development of novel vibration damping devices in vehicles.

KEYWORDS

nonlinear energy sink, cubic stiffness, nonlinear damping, half-vehicle model, genetic algorithm

1 Introduction

The Nonlinear Energy Sink (NES) was first proposed by Vakakis. (2001) and Gendelman et al. (2001) in 2001 as a novel type of nonlinear passive vibration absorber. A typical NES consists of a cubic nonlinear stiffness element, a damper, and a mass block (Xiong et al., 2015). Its most distinguishing feature is that the system does not possess a fixed natural frequency and can resonate with a wide spectrum of vibration components (Lu and Chen, 2017). This characteristic facilitates targeted energy transfer (TET) (Lu et al., 2020), providing a wide vibration suppression bandwidth and excellent energy dissipation performance. In recent years, NES configurations have evolved. For example, the integration of NES with multistable systems has led to the creation of broadband bistable isolators (Chen et al., 2025); and its combination with high-static-low-dynamic-stiffness (HSLDS) characteristics has improved vibration mitigation under low-frequency, high-amplitude excitations (Lu et al., 2017). Additionally, Wang et al. designed an inertially-enhanced asymmetric nonlinear energy sink (NES), demonstrating superior vibration suppression under harmonic and seismic excitations, and exhibiting robust performance against excitation variations. In the area of novel structures and multifunctional designs (Wang et al., 2022), Liu et al. proposed a NES that combines an Euler-buckling beam with a piezoelectric energy harvester, achieving synergistic optimization of vibration suppression and energy harvesting (Liu et al., 2025).

However, traditional NES devices generally rely on physical mass blocks for energy absorption, resulting in bulky structures that are unsuitable for applications requiring lightweight designs, such as in vehicles and aerospace systems. To address this limitation, inertial elements were introduced into the NES framework, giving rise to Inerter-Based Nonlinear Energy Sinks (INES). The inerter is a two-terminal mechanical element that amplifies equivalent inertia through compact mechanical designs, achieving lightweight construction without sacrificing energy absorption capability. Zhang et al. (2019) proposed an INES configuration consisting of a damper, a nonlinear spring, and a parallelly connected inerter, demonstrating excellent energy dissipation and vibration control performance. Wang et al. (2024a) applied INES to a half-vehicle system, significantly reducing dynamic loads and deflections of the front and rear tires. Javidialesaadi and Wierschem. (2019) connected the inerter between the mass block and the fixed point in the NES, effectively suppressing the dynamic response of the primary structure. Furthermore, Wang et al. (2024b) conducted a detailed study on the dynamic performance and parameter optimization of a half-vehicle system coupled with an inerter-based X-structure nonlinear energy sink, highlighting its enhanced vibration control capabilities. Subsequent research has explored various INES configurations and their applications in different engineering contexts, continually enriching the theoretical and practical framework of inerter-based nonlinear energy sinks.

Nevertheless, most current studies on NES and INES still rely on linear damping (as shown in Table 1), which poses performance limitations in practical applications (Lamarque et al., 2011; Huang et al., 2024). Vakakis (Saeed et al., 2020) pointed out that excessive damping prematurely terminates the TET process, reducing energy dissipation efficiency, whereas insufficient damping prevents timely dissipation of incoming energy, potentially leading to energy backflow. In contrast, nonlinear damping features amplitude-frequency adaptive characteristics: it provides weak damping at low energy levels to sustain TET and enhances dissipation at high energy levels to suppress backflow, thereby offering clear advantages in dynamic control. Moreover, the nonlinear stiffness elements traditionally used in NES have their own drawbacks, such as tuning difficulty and the tendency to induce multistability or even chaotic dynamics, which limits system controllability and stability under varying operating conditions. Therefore, exploring energy dissipation structures that do not rely on nonlinear stiffness and instead utilize nonlinear damping as the primary mechanism holds significant engineering and theoretical value.

Existing studies have shown that nonlinear damping NES exhibits good performance under single-degree-of-freedom (SDOF) and harmonic excitation conditions. Bi et al. (2002) applied shock absorbers with nonlinear damping to the rear suspension system of vehicles and found that it was beneficial in reducing the root-mean-square (RMS) value of body vibration acceleration and the relative dynamic load between the wheels and the road surface. Zhang and Kong. (2023); Zhang et al., 2023) investigated the vibration suppression performance of SDOF NES with nonlinear damping under harmonic excitation and found that NES systems with combined nonlinear damping exhibited better vibration suppression under simple harmonic excitation. Li. (2015) replaced the linear damping in NES with nonlinear damping and found that NES systems with nonlinear damping had a broader bandwidth of strongly modulated responses, indicating superior broadband vibration suppression characteristics. Umair and Hou. (2024) pointed out that increasing nonlinear damping can significantly reduce the peak displacement transmissibility in the resonance region without significantly

TABLE 1 Comparison of conventional NES, INES and Inertially-Enhanced Damping Energy Sink (IDES).

Characteristics	Traditional NES	INES (existing studies)	IDES (this paper)
Stiffness characteristics	Cubic nonlinearity	Cubic nonlinearity	Linear
Damping characteristics	Linear damping	Linear damping	Nonlinear damping
Inertial	NO	Yes	Yes
Energy dissipation mechanism	Tiffness nonlinear resonance capture	Inertial amplification + stiffness nonlinear	Nonlinear damped energy dissipation + inertial synergy
Key benefits	Wideband energy transfer	Lightweight	Amplitude-frequency adaptive

affecting high-frequency performance. Similarly, under force excitation, the increase in nonlinear damping significantly reduced the peak force transmissibility in the resonance zone while maintaining high-frequency isolation performance. Philip et al. (2023) found that for NES with nonlinear damping, the external excitation required to trigger saddle-node bifurcation was greatly reduced.

However, the current literature mainly focuses on SDOF systems and idealized excitations (such as harmonic or impulsive excitation). Research on the mechanism of nonlinear damping NES or INES in multi-degree-of-freedom (MDOF) coupled structures (such as pitch-vertical motion in vehicles) and under random excitation conditions remains relatively scarce. In recent years, some researchers have attempted to introduce NES into half-vehicle models to verify its practical application value in coupled vibration control, such as designing nonlinear energy sinks in half-vehicle systems to simultaneously regulate vertical and pitch responses (Wang et al., 2025). However, the internal nonlinear coordination mechanisms have not yet been fully revealed.

Based on this, this paper proposes a novel Inerter-Enhanced Damping Energy Sink (IDES), focusing on its vibration suppression potential and energy synergistic mechanisms in multi-degree-of-freedom coupled systems. To systematically evaluate the performance of IDES in complex dynamic environments, this study will develop a half-car coupled dynamic model, derive its motion equations, and perform numerical simulations using the Simulink platform to accurately capture the influence of nonlinear damping and inertial effects on the system response.

The structure of this paper is as follows: In Section 2, the modeling process of four IDES configurations (Types I–IV) will be described in detail, and their dynamic responses under harmonic excitation will be analyzed using the Harmonic Balance Method (HBM) and Pseudo-Arc Length Method (PALM) to select the optimal configuration. In Section 3, the optimal configuration will be applied to the half-car system, and the half-car system model will be established. In Section 4, the excitation boundaries will be described, and evaluation metrics for the subsequent vibration reduction performance of the half-car system will be constructed. In Section 5, the dynamic response of the half-car system with IDES under road harmonic excitation will be analyzed using HBM and PALM, and its dynamic performance will be further investigated under random road excitation. A genetic algorithm will be employed to optimize the structural parameters of IDES, and comparisons will be made with traditional suspension systems and optimized INES suspension systems. Finally, Section 6 concludes the paper.

2 Dynamic performance analysis of single-degree-of-freedom coupled IDES suspension system

2.1 Modeling of single-degree-of-freedom suspension system

According to the configurations of inerter, nonlinear damping, and linear springs, four single-degree-of-freedom suspension system models with different IDES (Inerter-based Dynamic Energy Suspension) configurations were designed. The nonlinear dynamic equations of these systems were established using Newton's second law. Subsequently, the HBM-PALM was employed to solve the dynamic responses of these four suspension systems under harmonic excitation, thereby analyzing their dynamic performance.

The distinctions among Coupled Hybrid Type I, II, and III IDES primarily derive from the configuration of the linear spring, nonlinear damping, and inerter within the system, as illustrated in Figure 1.

Type I: Vertically installed on the suspension by connecting a linear spring and a nonlinear damper in parallel, which are then connected in series with an inerter.

Type II: Vertically installed on the suspension by connecting an inerter with a parallel combination of a linear spring and a nonlinear damper.

Type III: Vertically installed on the suspension by connecting an inerter and a nonlinear damper in parallel, which are then connected in series with a linear spring.

Type IV: Vertically installed on the suspension by connecting a linear spring in series with a parallel combination of a nonlinear damper and an inerter.

A harmonic excitation (Acos(ωt)) is applied to the base to investigate the vibration attenuation performance of the suspension system, where A denotes the excitation amplitude, ω the excitation frequency, z_2 the vertical displacement of the suspension, z_1 the vertical displacement of the base, and z_b the vertical displacement of the IDES inerter. The specific structural parameters are listed in Table 2.

Using Newton's second law, the displacement dynamic equations for the suspension system with the coupled hybrid type I IDES, and the IDES, can be derived as Equation 1.

$$\begin{aligned} &mz_2'' + c_1(z_2' - z_1') + c_2(z_2' - z_b')(z_2 - z_b)^2 + k_1(z_2 - z_1) \\ &\quad + k_2(z_2 - z_b) = 0 \\ &b(z_b'' - z_1'') - k_2(z_2 - z_b) - c_2(z_2' - z_b')(z_2 - z_b)^2 = 0 \end{aligned} \tag{1}$$

The displacement dynamics equations for the suspension system of the coupled hybrid II IDES and the displacement dynamics equations for the IDES are

$$\begin{aligned} &mz_2'' + c_1(z_2' - z_1') + k_1(z_2 - z_1) + b(z_2'' - z_b'') = 0 \\ &b(z_2'' - z_b'') - k_2(z_b - z_1) - c_2(z_b' - z_1')(z_b - z_1)^2 = 0 \end{aligned} \tag{2}$$

The displacement dynamics equations for the suspension system of the coupled hybrid III IDES and the displacement dynamics equations for the IDES are

$$\begin{aligned} &mz_2'' + c_1(z_2' - z_1') + c_2(z_2' - z_b')(z_2 - z_b)^2 + k_1(z_2 - z_1) \\ &\quad + b(z_2 - z_b) = 0 \\ &b(z_2'' - z_b'') - k_2(z_b - z_1) - c_2(z_2' - z_b')(z_2 - z_b)^2 = 0 \end{aligned} \tag{3}$$

The displacement dynamics equations for the suspension system of the coupled hybrid type IV IDES and the displacement dynamics equations for the IDES are

$$\begin{aligned} &mz_2'' + c_1(z_2' - z_1') + k_1(z_2 - z_1) + k_2(z_2 - z_b) = 0 \\ &b(z_b'' - z_1'') + k_2(z_b - z_2) + c_2(z_b' - z_1')(z_b - z_1)^2 = 0 \end{aligned} \tag{4}$$

In the dynamic Equations 1–4,the mass term mz_2'' is expressed using absolute acceleration because Newton's second law must be applied in an inertial reference frame. The effects of base motion (such as z_1 and z_b) are transmitted to the mass through the relative displacements or velocities of the springs and dampers, ensuring

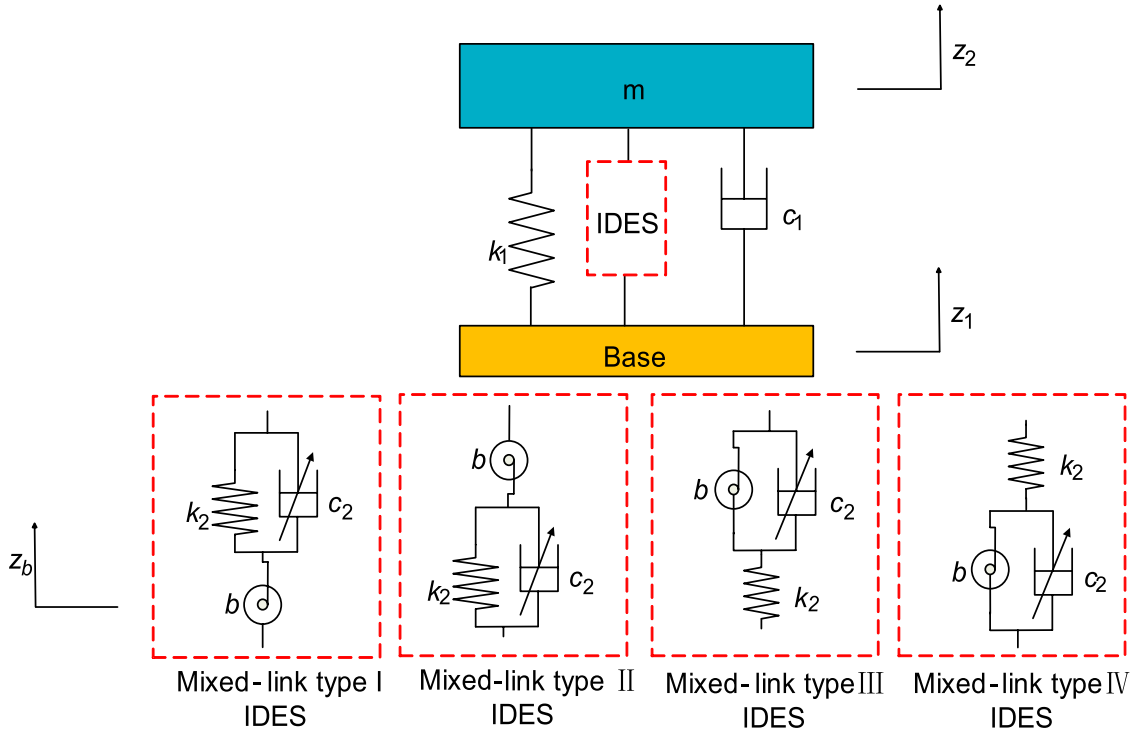

FIGURE 1
Four IDES coupled suspension models.

TABLE 2 Structural parameters of the suspension system with coupled IDES.

Symbol	Structural parameter	Unit
m	Suspension mass	kg
c1	Suspension damper damping coefficient	Ns/m
k1	Suspension spring stiffness coefficient	N/m
c2	IDES damper nonlinear damping coefficient	Ns/m^3
k2	IDES spring stiffness coefficient	N/m
b	IDES inerter inertial coefficient	kg

that the mass response in the inertial frame is correctly coupled with the base motion and avoiding any physical inconsistency.

To realize the displacement-modulated nonlinear damping mechanism described in Equations 1–4, $c(x_1 - x_2)^2(v_1 - v_2)$, a passive hydraulic damper with specially designed flow channels can be employed as the actuating element. In this model, the squared relative displacement term $(x_1 - x_2)^2$ acts as a modulation function and, together with the coefficient c, constitutes a transient effective damping coefficient, causing the damping force to increase quadratically with the deformation amplitude. In such a passive hydraulic damper, the flow area of the throttle valve can be mechanically designed to vary quadratically with the piston displacement, thereby directly achieving the displacement-dependent nonlinear damping behavior without the need for external control.

2.2 Dynamic response and vibration isolation performance analysis of four IDES suspension systems

The dynamic response of the four IDES suspension systems is obtained using the HBM-PALM method. The Harmonic Balance Method (HBM) is a powerful tool for analyzing the steady-state response of nonlinear vibration systems. It represents the system's dynamic response as a series of harmonic components, transforming the problem into solving a set of algebraic equations. Due to the nonlinear nature of the system, only low-order harmonics (such as the first-order harmonic) are typically retained as an approximate solution, and higher-order harmonic terms are ignored. This method provides significant advantages in simplifying the analysis of nonlinear vibrations, especially for vibration control

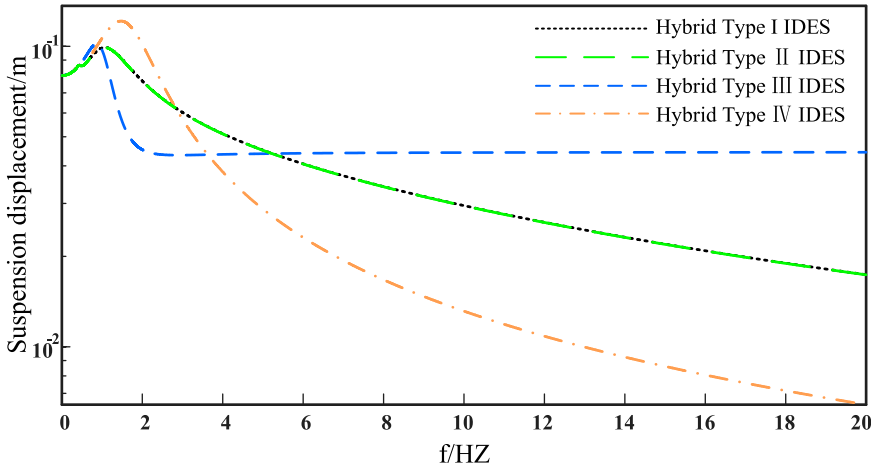

FIGURE 2
Comparison of dynamic characteristics of four suspension systems under simple harmonic excitation. (A = 0.08, v = 15m/s, k_1 = 8000N/m, c_1 = 800Ns/m, k_2 = 1000N/m, c_2 = 1 × $10^6 Ns/m$).

problems such as suspension systems. The Pseudo-Arc Length Method (PALM) is a numerical method commonly used to solve the steady-state solutions of nonlinear systems. By introducing a pseudo-arc length parameter, it avoids the branch switching failure that may occur in conventional arc length methods, effectively tracking multiple solutions of the nonlinear system. In the analysis presented here, PALM is combined with HBM to precisely track the dynamic response of the complex nonlinear system under different operating conditions.

Since Equations 1–3 all contain cubic nonlinear terms, higher-order harmonic terms can be omitted, retaining only the first-order harmonic as an approximate solution. The solutions for the suspension displacement z_1 and IDES displacement z_b are assumed to be

$$Z = \begin{pmatrix} z_2 \\ z_b \end{pmatrix} = \begin{pmatrix} a_1 \cos(\omega t) + a_2 \sin(\omega t) \\ b_1 \cos(\omega t) + b_2 \sin(\omega t) \end{pmatrix} \tag{5}$$

Substituting Equation 5 into Equations 1–4 and balancing the parameters for the oscillatory terms cos(ωt) and sin(ωt) leads to a set of nonlinear algebraic equations, which are given by Equation 6.

$$Q(a_1, a_2, b_1, b_2, \omega) = 0 \tag{6}$$

Equation 5 includes four nonlinear equations governing the dynamic behavior of the coupled IDES half-car system. To resolve the dimensional deficiency of the system, an arc-length parameter is introduced, extending the problem into a 5-dimensional space, formulated as Equation 7.

$$\mathrm{Y} = [a_1, a_2, b_1, b_2, \omega]^{\mathrm{T}} \tag{7}$$

At this point the system of equations can be expressed as Equation 8.

$$D(Y, s) = 0 \tag{8}$$

At this point the system of equations has 5 equations, and constraints should be imposed in order to avoid the folding point of the solution

$$\varepsilon \cdot \Delta Y - \Delta s = 0 \tag{9}$$

Equation 9 can be transformed into the Cauchy problem

$$\frac{\mathrm{d}Y}{\mathrm{d}s} = \varepsilon(Y_0), Y(0) = Y_0 \tag{10}$$

Equation 10 can be used to calculate the corresponding predictive solution using the modified Eulerian method

$$Y_j = Y_{j-1} + \varepsilon\left(Y_{j-1}\right)\left(s_j - s_{j-1}\right) + \frac{\left(s_j - s_{j-1}\right)^2}{2} \cdot \frac{\varepsilon\left(Y_{j-1}\right) - \varepsilon\left(Y_{j-2}\right)}{s_{j-1} - s_{j-2}}, \quad j = 1, 2, \ldots \tag{11}$$

Newton-type iterative corrections defined in Equation 12 can be used to control the accuracy of the solution.

$$Y_j^0 = Y_j, Y_j^n = Y_j^{n-1} - \begin{bmatrix} DQ\left(Y_j\right) \\ P\left(Y_j\right) \end{bmatrix}^{-1} \begin{bmatrix} Q\left(Y_j^{n-1}\right) \\ 0 \end{bmatrix}, \quad n = 1, 2, \ldots \tag{12}$$

Through a limited series of iterations, variable Y^* (derived from solving Equations 10, 11 asymptotically approaches a state fulfilling condition $Q(Y^*) = 0$. The resulting equilibrium magnitudes induced by harmonic roadway vibrations are

$$Z_m = \begin{pmatrix} z_1 \\ z_b \end{pmatrix} = \begin{pmatrix} \sqrt{a_1^2 + a_2^2} \\ \sqrt{b_1^2 + b_2^2} \end{pmatrix} \tag{13}$$

As shown in Figure 2, the suspension dynamic displacements of the coupled suspension systems with four different IDES configurations under harmonic excitation are illustrated. It can be observed that the displacement curves of the hybrid type I and type II overlap. This is because, although the mechanical connection forms differ between hybrid type I and hybrid type II, the linear spring and nonlinear damper always form an equivalent parallel branch with the inerter, and the other end of this branch is fixed to the base. Therefore, under harmonic excitation, the motion equations of the suspension mass can be transformed into the same

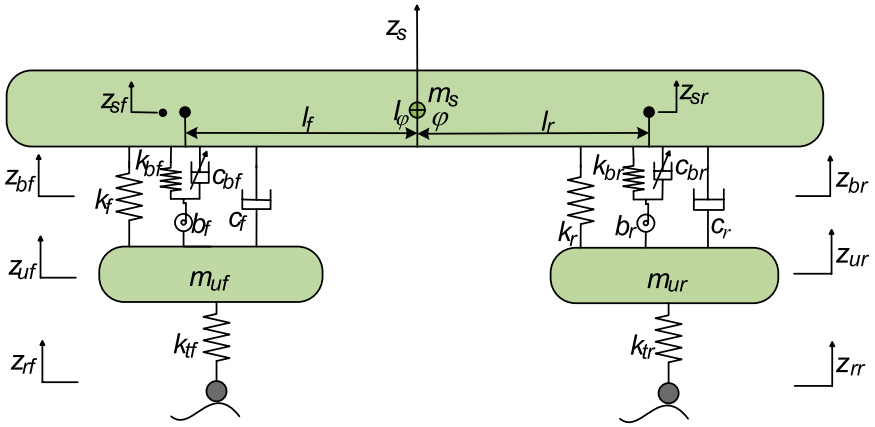

FIGURE 3
Half-car model combined with IDES.

TABLE 3 Structural parameters of the half-car system.

m_s	I_φ	m_{uf}	m_{ur}	l_f
$690kg$	$1222kgm^2$	$40kg$	$45kg$	$1.3m$
k_r	c_f	c_r	k_{tf}	k_r
$22000N/m$	$1000Ns/m$	$1000Ns/m$	$200000N/m$	$22000N/m$

form in the frequency domain, exhibiting equivalent dynamic effects and resulting in identical suspension responses.

In contrast, the connection patterns of hybrid type III and type IV alter the force transmission paths: in hybrid type III, the nonlinear damper and inerter are connected in parallel and directly coupled with the suspension, whereas in hybrid type IV, a linear spring serves as an intermediary, making the inerter and damper indirectly coupled to the suspension. This structural difference changes the acting points of the inertial and damping forces relative to the base, thereby leading to distinct frequency response characteristics. Consequently, the suspension dynamic responses of hybrid type III and type IV under harmonic excitation are not identical.

In summary, compared to the other two systems, the coupled suspension systems with hybrid type I and hybrid type II IDES exhibit smaller resonance peaks in suspension displacement. Since hybrid type I and type II are dynamically equivalent, the hybrid type I IDES suspension system is selected for subsequent coupling with the half-car system in the next section.

3 Half-car modeling in conjunction with IDES

The suspension system of the coupled hybrid type I IDES is applied to the half-car model shown in Figure 3. The vehicle body connects to the front and rear tires through four junction points. Its dynamic response includes uncoupled bounce and pitch modes, while tires exhibit vertical compliance relative to the body. Deployed in parallel with suspension elements, IDES actuators bridge the body-tire assemblies to attenuate induced oscillations. m_s is the body mass; I_ϕ is the body pitch inertia; m_{uf} and m_{ur} are the front and rear tire masses, respectively; The stiffness and damping coefficients for the front and rear suspensions are denoted by $k_f\,(k_r)$ and $c_f\,(c_r)$, respectively; Front and rear tire stiffnesses are denoted by k_{tf} and k_{tr}, respectively; $b_f\,(b_r)$ defines the inertial parameter of the front IDES, $k_{bf}\,(k_{br})$ its linear rigidity, and $c_{bf}\,(c_{br})$ the nonlinear damping factor for the rear IDES; l_f, l_r are the distances from the front and rear axles to the body center, respectively; z_s, z_{sf} and z_{sr} are the displacements of the body center, front and rear, respectively; φ is the body pitch angle; z_{uf}, z_{ur} are the displacements of the front and rear tires, respectively; z_{bf} and z_{br} are the displacements of the front and rear IDES junctions P_f and P_r, respectively; The road excitation profiles for the front and rear wheels are defined by z_{rf} and z_{rr}, correspondingly. The half-car system's key structural attributes are detailed in Table 3 (Zhang et al., 2022; Lamarque et al., 2011; Du and Zhang, 2008).

Based on Newton's second law, the dynamic equations of a half-car model combined with IDES were derived around the static equilibrium positions of the vehicle body and the front and rear tires. The vertical and pitch dynamic equations of the vehicle body are as follows

$$\begin{aligned} m_s z_s'' &+ c_f\left(z_{sf}' - z_{uf}'\right) + c_r\left(z_{sr}' - z_{ur}'\right) + k_f\left(z_{sf} - z_{uf}\right) + k_r\left(z_{sr} - z_{ur}\right) \\ &+ c_{bf}\left(z_{sf}' - z_{bf}'\right)\left(z_{sf} - z_{bf}\right)^2 + c_{br}\left(z_{sr}' - z_{br}'\right)\left(z_{sr} - z_{br}\right)^2 \\ &+ k_{br}\left(z_{sr} - z_{br}\right) + k_{bf}\left(z_{sf} - z_{bf}\right) = 0 \end{aligned} \tag{14}$$

$$\begin{aligned} I_\varphi \varphi'' &+ c_r l_r\left(z_{sr}' - z_{ur}'\right) - c_f l_f\left(z_{sf}' - z_{uf}'\right) + k_r l_r\left(z_{sr} - z_{ur}\right) \\ &- k_f l_f\left(z_{sf} - z_{uf}\right) + c_{br} l_r\left(z_{sr}' - z_{br}'\right)\left(z_{sr} - z_{br}\right)^2 \\ &- c_{bf} l_f\left(z_{sf}' - z_{bf}'\right)\left(z_{sf} - z_{bf}\right)^2 + k_{br} l_r\left(z_{sr} - z_{br}\right) \\ &- k_{bf} l_f\left(z_{sf} - z_{bf}\right) = 0 \end{aligned} \tag{15}$$

The dynamic equations for the front and rear tires are

$$\begin{aligned} m_{uf} z_{uf}'' &- b_f\left(z_{bf}'' - z_{uf}''\right) - c_f\left(z_{sf}' - z_{uf}'\right) - k_f\left(z_{sf} - z_{bf}\right) \\ &+ k_{tf}\left(z_{uf} - z_{rf}\right) = 0 \end{aligned} \tag{16}$$

$$\begin{aligned} m_{ur} z_{ur}'' &- b_r\left(z_{br}'' - z_{ur}''\right) - c_r\left(z_{sr}' - z_{ur}'\right) - k_r\left(z_{sr} - z_{br}\right) \\ &+ k_{tr}\left(z_{ur} - z_{rr}\right) = 0 \end{aligned} \tag{17}$$

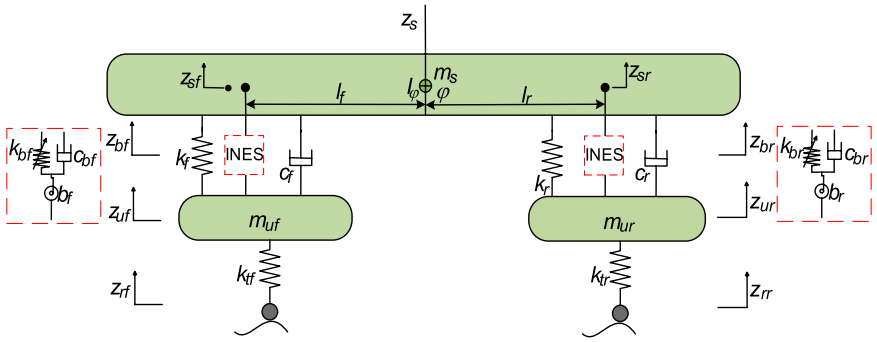

FIGURE 4
Half-car model combined with INES.

The dynamic equations for the two IDES positioned between the body and the tires are

$$b_f\left(z''_{bf} - z''_{uf}\right) - c_{bf}\left(z'_{sf} - z'_{bf}\right)\left(z_{sf} - z_{bf}\right)^2 + k_{bf}\left(z_{bf} - z_{sf}\right) = 0 \tag{18}$$

$$b_r\left(z''_{br} - z''_{ur}\right) - c_{br}\left(z'_{sr} - z'_{br}\right)\left(z_{sr} - z_{br}\right)^2 + k_{br}\left(z_{br} - z_{sr}\right) = 0 \tag{19}$$

As shown in Figure 3, if the pitch angle of the car is small, the front-back displacement of the car can be expressed as

$$\begin{aligned} z_{sf} &= z_s - l_f \sin\phi \approx z_s - l_f\phi \\ z_{sr} &= z_s + l_r \sin\phi \approx z_s + l_r\phi \end{aligned} \tag{20}$$

Substituting Equation 20 into Equations 14, 19 can be further written in matrix form

$$MZ'' + CZ' + KZ + H(Z) = F \tag{21}$$

In Equation 21, M symbolizes the mass matrix, C represents the damping matrix, K is the stiffness matrix, H(Z) corresponds to the nonlinear term matrix, F stands for the excitation matrix, and Z denotes the displacement matrix, as specified by Equation 22.

$$M = \begin{pmatrix} m_s & 0 & 0 & 0 & 0 & 0 \\ 0 & I_\varphi & 0 & 0 & 0 & 0 \\ 0 & 0 & m_{uf} + b_f & 0 & -b_f & 0 \\ 0 & 0 & 0 & m_{ur} + b_r & 0 & -b_r \\ 0 & 0 & -b_f & 0 & b_f & 0 \\ 0 & 0 & 0 & -b_r & 0 & b_r \end{pmatrix}$$

$$C = \begin{pmatrix} c_f + c_r & c_r l_r - c_f l_f & -c_f & -c_r & 0 & 0 \\ c_r l_r - c_f l_f & c_r l_r^2 + c_f l_f^2 & c_f l_f & -c_r l_r & 0 & 0 \\ -c_f & c_f l_f & c_f & 0 & 0 & 0 \\ -c_r & -c_r l_r & 0 & c_r & 0 & 0 \\ 0 & 0 & 0 & 0 & 0 & 0 \\ 0 & 0 & 0 & 0 & 0 & 0 \end{pmatrix}$$

$$K = \begin{pmatrix} k_f + k_r + k_{bf} + k_{br} & k_r l_r - k_f l_f + k_{br} l_r - k_{bf} l_f & -k_f & -k_r & -k_{bf} & -k_{br} \\ k_r l_r - k_f l_f + k_{br} l_r - k_{bf} l_f & k_r l_r^2 + k_f l_f^2 + k_{br} l_r^2 + k_{bf} l_f^2 & k_f l_f & -k_r l_r & k_{bf} l_f & -k_{br} l_r \\ -k_f & k_f l_f & k_f + k_{tf} & 0 & 0 & 0 \\ -k_r & -k_r l_r & 0 & k_r + k_{tr} & 0 & 0 \\ -k_{bf} & k_{bf} l_f & 0 & 0 & k_{bf} & 0 \\ -k_{br} & -k_{br} l_r & 0 & 0 & 0 & k_{br} \end{pmatrix}$$

$$H(Z) = \begin{pmatrix} c_{bf}\left(z'_s - l_f\varphi' - z'_{bf}\right)\left(z_s - l_f\varphi - z_{bf}\right)^2 + c_{br}\left(z'_s + l_r\varphi' - z'_{br}\right)\left(z_s + l_r\varphi - z_{br}\right)^2 \\ c_{br} l_r\left(z'_s + l_r\varphi' - z'_{br}\right)\left(z_s + l_r\varphi - z_{br}\right)^2 - c_{bf} l_f\left(z'_s - l_f\varphi' - z'_{bf}\right)\left(z_s - l_f\varphi - z_{bf}\right)^2 \\ 0 \\ 0 \\ -c_{bf}\left(z'_s - l_f\varphi' - z'_{bf}\right)\left(z_s - l_f\varphi - z_{bf}\right)^2 \\ -c_{br}\left(z'_s + l_r\varphi' - z'_{br}\right)\left(z_s + l_r\varphi - z_{br}\right)^2 \end{pmatrix}$$

$$F = \begin{pmatrix} 0 \\ 0 \\ k_{tf} z_{rf} \\ k_{tr} z_{rr} \\ 0 \\ 0 \end{pmatrix} \quad Z = \begin{pmatrix} z_s \\ \phi \\ z_{uf} \\ z_{ur} \\ z_{bf} \\ z_{br} \end{pmatrix} \tag{22}$$

A comparative assessment of dynamic performance was conducted across three configurations: the baseline half-vehicle system, its INES-integrated counterpart, and the reference model. Subsequent analysis derived the governing equations for the original suspension assembly, given by Equation 23.

$$\begin{aligned} &m_s z''_s + c_f\left(z'_{sf} - z'_{uf}\right) + c_r\left(z'_{sr} - z'_{ur}\right) + k_f\left(z_{sf} - z_{uf}\right) \\ &\quad + k_r\left(z_{sr} - z_{ur}\right) = 0 \\ &I_\varphi\varphi'' + c_r l_r\left(z'_{sr} - z'_{ur}\right) - c_f l_f\left(z'_{sf} - z'_{uf}\right) + k_r l_r\left(z_{sr} - z_{ur}\right) \\ &\quad - k_f l_f\left(z_{sf} - z_{uf}\right) = 0 \\ &m_{uf} z''_{uf} - c_f\left(z'_{sf} - z'_{uf}\right) - k_f\left(z_{sf} - z_{bf}\right) + k_{tf}\left(z_{uf} - z_{rf}\right) = 0 \\ &m_{ur} z''_{uf} - c_r\left(z'_{sr} - z'_{ur}\right) - k_r\left(z_{sr} - z_{br}\right) + k_{tr}\left(z_{ur} - z_{rr}\right) = 0 \end{aligned} \tag{23}$$

The suspension system with coupled INES is applied to the half-vehicle model as shown in Figure 4, where k_{bf} and k_{br}, c_{bf} and c_{br} represent the nonlinear stiffness and linear damping of the front and rear INES, respectively. The meanings of the other parameters are the same as those in Figure 3.

The dynamical equations for the coupling of the half-car system to the INES are given in Equation 24.

$$\begin{aligned} &m_s z''_s + c_f\left(z'_{sf} - z'_{uf}\right) + c_r\left(z'_{sr} - z'_{ur}\right) + k_f\left(z_{sf} - z_{uf}\right) + k_r\left(z_{sr} - z_{ur}\right) \\ &\quad + c_{bf}\left(z'_{sf} - z'_{bf}\right) + c_{br}\left(z'_{sr} - z'_{br}\right) + k_{br}\left(z_{sr} - z_{br}\right)^3 \\ &\quad + k_{bf}\left(z_{sf} - z_{bf}\right)^3 = 0 \\ &I_\varphi\varphi'' + c_r l_r\left(z'_{sr} - z'_{ur}\right) - c_f l_f\left(z'_{sf} - z'_{uf}\right) + k_r l_r\left(z_{sr} - z_{ur}\right) \\ &\quad - k_f l_f\left(z_{sf} - z_{uf}\right) + c_{br} l_r\left(z'_{sr} - z'_{br}\right) - c_{bf} l_f\left(z'_{sf} - z'_{bf}\right) \\ &\quad + k_{br} l_r\left(z_{sr} - z_{br}\right)^3 - k_{bf} l_f\left(z_{sf} - z_{bf}\right)^3 = 0 \\ &m_{uf} z''_{uf} - b_f\left(z''_{bf} - z''_{uf}\right) - c_f\left(z'_{sf} - z'_{uf}\right) - k_f\left(z_{sf} - z_{bf}\right) \\ &\quad + k_{tf}\left(z_{uf} - z_{rf}\right) = 0 \\ &m_{ur} z''_{ur} - b_r\left(z''_{br} - z''_{ur}\right) - c_r\left(z'_{sr} - z'_{ur}\right) - k_r\left(z_{sr} - z_{br}\right) \\ &\quad + k_{tr}\left(z_{ur} - z_{rr}\right) = 0 \\ &b_f\left(z''_{bf} - z'_{uf}\right) - c_{bf}\left(z'_{sf} - z'_{bf}\right) + k_{bf}\left(z_{bf} - z_{sf}\right)^3 = 0 \\ &b_r\left(z''_{br} - z''_{ur}\right) - c_{br}\left(z'_{sr} - z'_{br}\right) + k_{br}\left(z_{br} - z_{sr}\right)^3 = 0 \end{aligned} \tag{24}$$

The dynamic equations of the three half-car systems derived here will be used for system modeling in subsequent sections to further investigate the specific vibration damping performance of each system.

4 Design of incentive boundaries and evaluation indicators

4.1 Description of the incentive boundary

The road surface simple harmonic excitation is the periodic vibration excitation caused by the uneven road surface when the vehicle is traveling on the road. Subjecting fore and aft tires to harmonic road excitations, the frequency-domain dynamics of the IDES-integrated half-car system are analyzed. Applied to the leading wheels, periodic pavement excitations are mathematically represented by Equation 25.

$$z_{rf} = A\cos(\omega t) \tag{25}$$

The rear tires experience identical harmonic road excitation to the front tires in amplitude (A) and angular frequency (ω), but with a phase delay of (l_f + l_r)/v, where v denotes the longitudinal vehicle velocity, as described in Equation 26.

$$z_{rr} = A\cos\left[\omega\left(t - \frac{l_f + l_r}{v}\right)\right] \tag{26}$$

Featuring cubic nonlinearities per Equations 14–19, the IDES-enhanced half-car model derives dynamic responses using HBM-PALM (Wang et al., 2014; Wu and Tang, 2022). Partitioned co-simulation (Hollari et al., 2014; Rahikainen et al., 2020) offers subsystem-decoupling advantages for real-time multi-physics systems. The spectral solution converges to first-harmonic approximations

$$\mathrm{Z} = \begin{pmatrix} z_s \\ \phi \\ z_{uf} \\ z_{ur} \\ z_{bf} \\ z_{br} \end{pmatrix} = \begin{pmatrix} a_1\cos(\omega t) + a_2\sin(\omega t) \\ b_1\cos(\omega t) + b_2\sin(\omega t) \\ c_1\cos(\omega t) + c_2\sin(\omega t) \\ d_1\cos(\omega t) + d_2\sin(\omega t) \\ e_1\cos(\omega t) + e_2\sin(\omega t) \\ g_1\cos(\omega t) + g_2\sin(\omega t) \end{pmatrix} \tag{27}$$

Substituting Equation 27 into Equations 13–18 and balancing the coefficients of harmonic terms $\cos(\omega t)$ and $\sin(\omega t)$ yields

$$\begin{aligned}
&F_1(a_1,\cdots g_1,a_2,\cdots g_2,\omega)\cos(\omega t)\\
&\quad + F_2(a_1,\cdots g_1,a_2,\cdots g_2,\omega)\sin(\omega t) = 0\\
&F_3(a_1,\cdots g_1,a_2,\cdots g_2,\omega)\cos(\omega t)\\
&\quad + F_4(a_1,\cdots g_1,a_2,\cdots g_2,\omega)\sin(\omega t) = 0\\
&F_5(a_1,\cdots g_1,a_2,\cdots g_2,\omega)\cos(\omega t)\\
&\quad + F_6(a_1,\cdots g_1,a_2,\cdots g_2,\omega)\sin(\omega t) = 0\\
&F_7(a_1,\cdots g_1,a_2,\cdots g_2,\omega)\cos(\omega t)\\
&\quad + F_8(a_1,\cdots g_1,a_2,\cdots g_2,\omega)\sin(\omega t) = 0\\
&F_9(a_1,\cdots g_1,a_2,\cdots g_2,\omega)\cos(\omega t)\\
&\quad + F_{10}(a_1,\cdots g_1,a_2,\cdots g_2,\omega)\sin(\omega t) = 0\\
&F_{11}(a_1,\cdots g_1,a_2,\cdots g_2,\omega)\cos(\omega t)\\
&\quad + F_{12}(a_1,\cdots g_1,a_2,\cdots g_2,\omega)\sin(\omega t) = 0
\end{aligned} \tag{28}$$

Nullification of harmonic coefficients in Equation 28 formulates the harmonic balance conditions

$$\begin{aligned}
&F_1(a_1,\cdots g_1,a_2,\cdots g_2,\omega)\cdots F_i(a_1,\cdots g_1,a_2,\cdots g_2,\omega)\\
&\cdots F_{12}(a_1,\cdots g_1,a_2,\cdots g_2,\omega) = 0
\end{aligned} \tag{29}$$

The mathematical formulations governing these twelve nonlinear equations are documented in the Appendix.

Equation 28 constitutes a twelve-equation nonlinear system governing the dynamic characteristics of the half-vehicle chassis integrated with IDES. Equation 28 has 13 parameters $(a_1,\cdots g_1,a_2,\cdots g_2,\omega)$, which may be expressed as Equation 30.

$$Q(X,\omega) = 0 \tag{30}$$

where $Q = [F_1,\cdots,F_{12}]^T$ and $X = [a_1,\cdots g_1,a_2,\cdots g_2,\omega]$, Equation 29 admits the reformulated representation as Equation 31.

$$Q(Y) = 0 \tag{31}$$

After a finite number of iteration steps, the solution of Equation 29 is obtained. The equilibrium vibrational magnitude induced by pavement periodic forcing converges to

$$\mathrm{Z}_m = \begin{pmatrix} z_{sm} \\ \phi_m \\ z_{ufm} \\ z_{urm} \\ z_{bfm} \\ z_{brm} \end{pmatrix} = \begin{pmatrix} \sqrt{a_1^2 + a_2^2} \\ \sqrt{b_1^2 + b_2^2} \\ \sqrt{c_1^2 + c_2^2} \\ \sqrt{d_1^2 + d_2^2} \\ \sqrt{e_1^2 + e_2^2} \\ \sqrt{g_1^2 + g_2^2} \end{pmatrix} \tag{32}$$

The vehicle tires experience random excitation originating from the road surface, which functions as the primary input force. The dynamic response characteristics of the IDES half-car system are subsequently analyzed using time-domain simulation. Furthermore, six critical evaluation metrics are utilized to quantify the root-mean-square (RMS) value associated with the system's dynamic response. The pavement-induced random excitation is inherently dependent on both the type of road surface and the vehicle's traveling speed. In this investigation, a Class C road profile is adopted, and the excitation is mathematically modeled through the filtered white noise method. Consequently, the stochastic excitation exerted on the front tires can be expressed as Equation 33.

$$z'_{rf}(t) = -2\pi f_0 z_{rf}(t) + 2\pi n_0\sqrt{G_q(n_0)v}\,\omega(t) \tag{33}$$

Here, f_0 represents the frequency, and $G_q(n_0)$ denotes the roughness coefficient of the pavement surface, c-level road profile to take $64\times10^{-6}m^3$; n_0 denotes the reference spatial frequency, set to $0.1m^{-1}$; vehicle speed v, set to $15m/s$; $\omega(t)$ represents a Gaussian white noise with a mean of 0 and an intensity of 1. Analogous to the harmonic excitation from the road surface, the random excitation applied to the rear tires of the vehicle exhibits a temporal lag compared to that of the front tires, which is mathematically expressed as Equation 34.

$$z_{rr}(t) = z_{rf}(t-\tau) \tag{34}$$

4.2 Evaluation system construction

Based on Equation 32, the dynamic behavior of the half-car system incorporating IDES is evaluated using a set of performance metrics, which include the vertical acceleration of the vehicle body

(z_s'', J_{VBVA}), pitch acceleration (ϕ'', J_{VBPA}), front suspension deflection $(z_{sf} - z_{uf}, J_{SDf})$, rear suspension deflection $(z_{sr} - z_{ur}, J_{SDr})$, front tire load fluctuation $(k_{tf}(z_{sf} - z_{uf}), J_{DTLf})$, and rear tire load fluctuation $(k_{tr}(z_{sr} - z_{ur}), J_{DTLr})$. The detailed formulations of these dynamic performance indicators are provided as follows

$$
\begin{aligned}
J_{VBVA} &= \omega^2 \sqrt{a_1^2 + a_2^2} \\
J_{VBPA} &= \omega^2 \sqrt{b_1^2 + b_2^2} \\
J_{SDf} &= \sqrt{\left(a_1 - l_f b_1 - c_1\right)^2 + \left(a_2 - l_f b_2 - c_2\right)^2} \\
J_{SDr} &= \sqrt{(a_1 + l_r b_1 - d_1)^2 + (a_2 + l_r b_2 - d_2)^2} \\
J_{DTLf} &= k_{tf} \sqrt{(c_1 - A)^2 + c_2^2} \\
J_{DTLr} &= k_{tr} \sqrt{\left(d_1 - A\cos\left(\omega \frac{l_f + l_r}{v}\right)\right)^2 + \left(d_2 - A\sin\left(\omega \frac{l_f + l_r}{v}\right)\right)^2}
\end{aligned} \tag{35}
$$

Given that the semi-car system's original model is based on linear dynamics, its response characteristics remain accessible through Laplace transform operations. Adopting a parallel algorithmic framework to the IDES-integrated configuration, vibrational outputs of both the original architecture and the INES-augmented system are resolved via the Harmonic Balance Method (HBM) and Pseudo-Arc Length Method (PALM) respectively, with all dynamic performance descriptors maintaining analytical consistency with Equation 35.

In this section, we have detailed the excitation boundaries of the half-car system and constructed relevant indicators for evaluating the system's vibration damping performance. These boundary conditions provide the foundation for the dynamic response analysis in the subsequent chapters, while the evaluation indicators will be used to assess the specific vibration damping performance of the system.

5 Dynamic characterization of IDES suspension system based on half-car

5.1 Dynamic performance study of pavement under simple harmonic excitation

Figure 5 illustrates the analytical dynamic behavior of the half-car system incorporating IDES through the combined HBM-PALM methodology. Assuming homogeneous tire configurations at both ends with equivalent structural properties, the vehicular velocity is maintained at 15 m/s as a moderate operational condition. Owing to the transient phase lag across axles, the displacement and pitch dynamics of the vehicle body manifest multi-band resonant behavior with periodic amplitude maxima. When the nonlinear damping of IDES is 1 × 106 N/m, the system's dynamic response becomes single-valued, demonstrating linear characteristics. At approximately 10 Hz, a distinct dynamic phenomenon can be observed: the vertical displacement of the vehicle body z_s and the pitch angle ϕ are nearly suppressed to zero, while the tire displacements $(z_{uf}, z_{ur})$and the inerter displacements within the front and rear suspension branches (z_{bf}, z_{br})exhibit peak responses. This behavior indicates the occurrence of a modal decoupling effect, in which the vibration energy is predominantly confined to the tire–suspension–inerter subsystem rather than being transmitted to the vehicle body. Consequently, the body motion is effectively isolated through a mechanism analogous to anti-resonance, where the primary system response approaches a minimum while the auxiliary subsystem undergoes large oscillations. In Figure 5, the analytical results are

Figure 6 shows the frequency-domain responses of six important dynamic performance metrics for the baseline half-car system, the system combined with INES, and the system combined with IDES under three operational speeds: 5 m/s (low speed), 15 m/s (mid-range speed), and 35 m/s (high speed). The assessment metrics include vertical acceleration of the vehicle body, pitch angular acceleration, dynamic deflection of both front and rear suspensions, and dynamic loading fluctuations on the front and rear tires.

As shown in Figures a and b, the frequency-domain responses of the vehicle body vertical acceleration and pitch angular acceleration under harmonic excitation in the half-vehicle system exhibit multiple resonance peaks. Particularly at low vehicle speeds, the low-frequency resonance phenomena become more pronounced, leading to an increase in the number of resonance peaks. This is due to the higher sensitivity of the suspension system to low-frequency excitations at low speeds, where the natural frequencies of the system align with the excitation frequencies, thereby generating more resonance peaks. At high vehicle speeds, the system's dynamic response shifts toward the high-frequency range, resulting in a reduction in the number of resonance peaks. Therefore, the appearance of multiple resonance peaks at low vehicle speeds is a natural consequence of the interaction between the system's inherent frequencies and low-frequency excitations, which is a normal phenomenon.

At low speed, compared to the original half-car system, the IDES-equipped system significantly suppresses resonance peaks in both suspension deflections and tire dynamic loads at the front and rear axles. Demonstrating excellent vibration reduction capability. However, as system damping rises overall, the maximum vertical and pitch accelerations of the vehicle body exhibit a small increase. Compared with the INES-integrated system, although the suspension and tire indicators are similar, the IDES system markedly reduces the peak values of vertical and pitch accelerations, indicating superior performance in ride comfort.

At medium speed, the IDES-integrated system continues to effectively suppress the resonance peaks of suspension deflection and tire dynamic loads. Compared with the INES system, IDES significantly mitigates the deterioration of vertical and pitch accelerations caused by the inerter, further demonstrating its synergistic advantage in mid-speed vibration control.

At high speed, the IDES system still effectively reduces the resonance responses of suspension deflection and tire dynamic loads while maintaining good control over the vertical acceleration of the vehicle body. Although the pitch acceleration resonance peak increases slightly, it is still significantly lower than that of the INES-integrated system, indicating that IDES can still balance stability and comfort at high speeds.

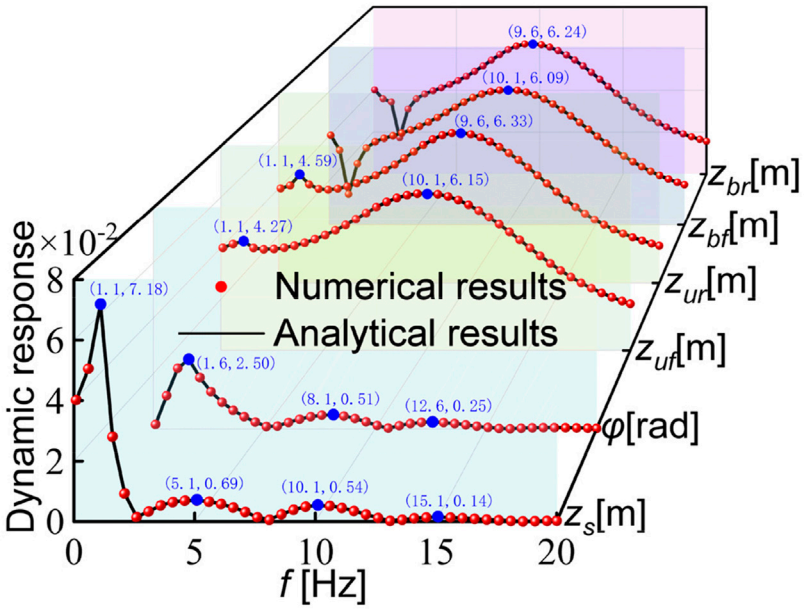

FIGURE 5
Comparison of the analytical and numerical outcomes for the dynamic response of the IDES half-car system under road harmonic excitation. ($A = 0.04m$, $b_f = b_r = 200kg$, $k_{bf} = k_{br} = 1 \times c_{bf} = c_{br} = 1 \times 10^6 Ns/m$).

Overall, the half-car system integrated with IDES exhibits favorable energy dissipation characteristics and coordinated dynamic responses across all speed conditions. Although the resonance peaks of suspension deflection and tire dynamic forces are somewhat higher than those of the INES system in certain cases, its suppression of vertical and pitch accelerations is significantly better, which is more conducive to achieving a balance between ride comfort and handling stability. In addition, compared to INES, IDES can effectively reduce the vertical acceleration and pitch angle acceleration of the vehicle body across a wide frequency range, significantly improving the vibration reduction performance of the vehicle body. Although the dynamic load on the front and rear tires and the dynamic deflection of the front and rear suspensions are slightly higher than those of INES in the same frequency band, the differences are minor and do not adversely affect the overall performance of the system. This shows that IDES achieves wide-band vibration reduction characteristics with relatively little cost through full-band optimization of the vehicle body's response.

When incorporating an inerter into the traditional NES to meet lightweight design requirements, a 1 kg ball screw inerter can achieve an adjustable inertance ranging from 60 to 240 kg (Smith, 2002).

5.2 Dynamic performance study of pavement under random excitation

The comparison of the vertical and pitch angular accelerations of the vehicle body for the baseline half-car system, the system combined with IDES, and the system combined with INES under road random excitation is shown in Figure 7. Table 4 provides the accurate RMS values for six evaluation metrics. When driven on a C-class pavement, metrics RMS(J_{VBVA}), RMS(J_{SDf}), RMS(J_{SDr}), RMS(J_{DTLf}), RMS(J_{DTLf}) and RMS(J_{DTLr}) of the IDES-equipped system are reduced by 0.69%, 5.75%, 5.56%, 6.07%, and 5.66%, respectively, compared to the original system, while metric RMS(J_{VBPA}) is slightly elevated by 1.94%, consistent with the road harmonic excitation scenario. Compared to the half-car system incorporating INES, IDES places greater emphasis on overall balance. In terms of "local" performance, it requires sacrificing some vibration suppression efficiency. For example, metrics RMS(J_{VBVA}) and RMS(J_{VBPA}) are reduced by 3.51% and 14.41%, respectively, significantly lowering the body pitch acceleration. However, metrics RMS(J_{SDf}), RMS(J_{SDr}), RMS(J_{DTLf}), and RMS(J_{DTLf}) show slight increases, though the magnitudes remain small. Furthermore, from an engineering application perspective, this balanced performance of IDES is more attractive, as vehicle suspension prioritizes "overall comfort and stability" rather than extreme optimization of individual metrics.

5.3 Optimized design of IDES suspension structure parameters

The parametric study reveals that applying the IDES structural parameters listed in Table 3 to the original suspension slightly degrades metric RMS(J_{VBPA}). To further enhance overall driver comfort, this study employs a genetic algorithm to optimize the structural parameters of the IDES suspension system, specifically stiffness, damping, and inertance coefficients. The optimization objective is to

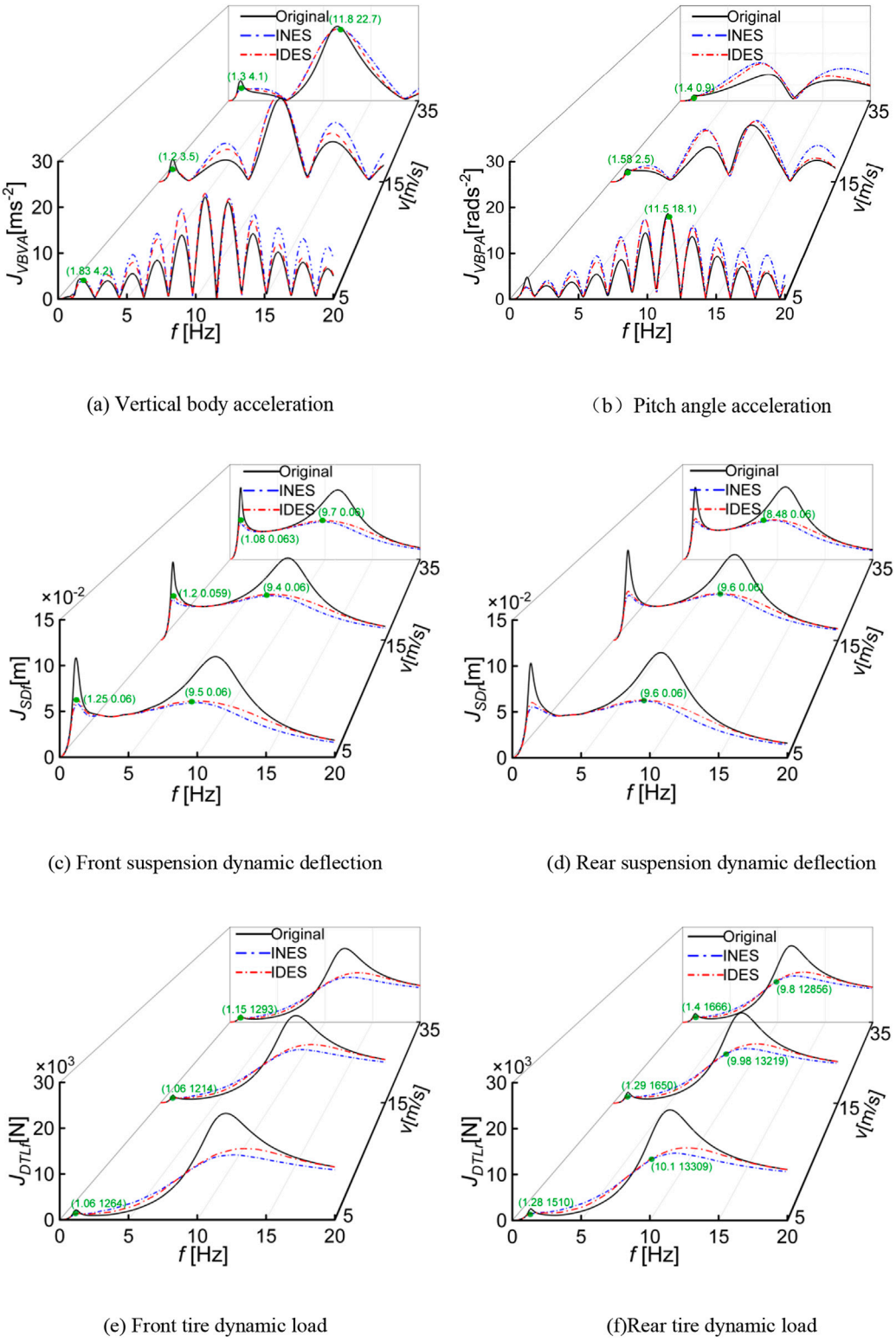

FIGURE 6
Comparison of vehicle dynamic performance metrics for the original half-vehicle model, the half-vehicle system equipped with INES, and the half-vehicle system incorporating IDES under harmonic excitation from the road surface. (A = 0.04m, b_f = b_r = 200kg; IDES: k_{bf} = k_{br} = 1 × 10^3N/m, c_{bf} = c_{br} = 1 × 10^6Ns/m^3; INES: k_{bf} = k_{br} = 1 × 10^6N/m, c_{bf} = c_{br} = 1 × 103 Ns/m;). **(a)** Vertical body acceleration. **(b)** Pitch angle acceleration. **(c)** Front suspension dynamic deflection. **(d)** Rear suspension dynamic deflection. **(e)** Front tire dynamic load. **(f)** Rear tire dynamic load.

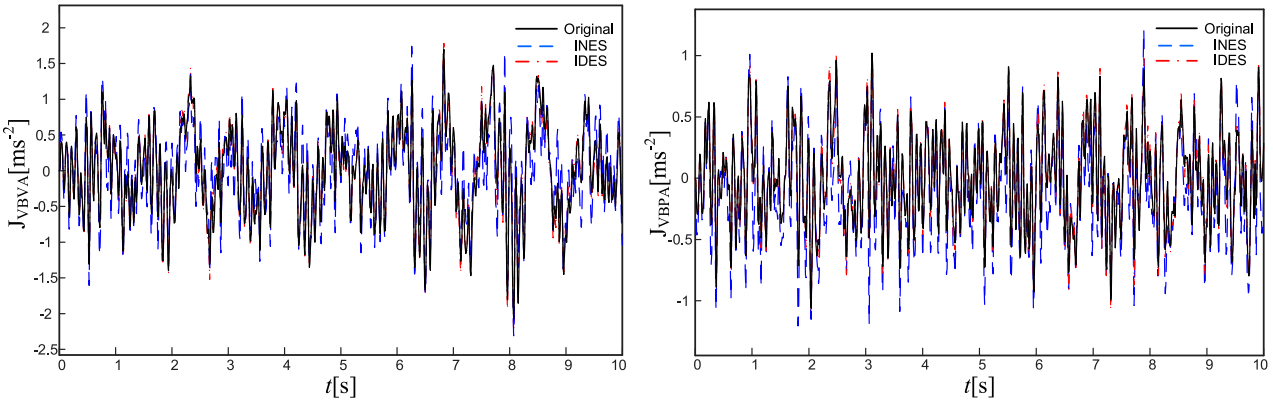

FIGURE 7
Comparison of body vertical and pitch angular accelerations for the original, IDES, and INES half-vehicle systems under random excitation (v = 15 m/s).

TABLE 4 RMS values of dynamic evaluation metrics under random excitation of pavements.

Dynamic performance indicators	Original	INES	Percentage of vibration reduction	IDES	Percentage of vibration reduction
$J_{VBVA}/(\mathrm{m}\cdot\mathrm{s}^{-2})$	0.5918	0.6091	−2.84%	0.5877	0.69%
$J_{VBPA}/(\mathrm{rad}\cdot\mathrm{s}^{-2})$	0.3817	0.4546	−16.04%	0.3891	−1.94%
$J_{SDf}/(\mathrm{m})$	0.0087	0.0072	17.24%	0.0082	5.75%
$J_{SDr}/(\mathrm{m})$	0.0090	0.0072	20%	0.0085	5.56%
$J_{DTLf}/(\mathrm{N})$	553.9300	482.0167	12.98%	520.2928	6.07%
$J_{DTLr}/(\mathrm{N})$	555.4266	472.8568	14.87%	524.0044	5.66%

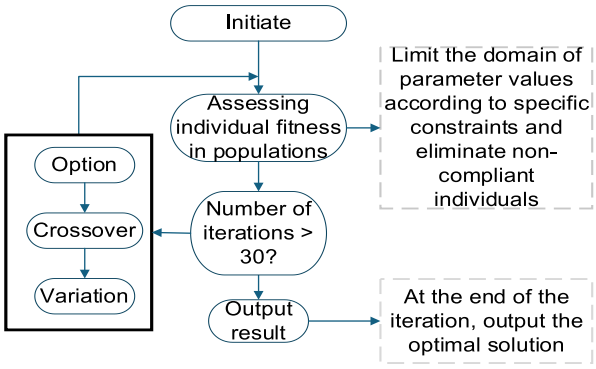

FIGURE 8
Optimization process using genetic algorithms.

improve metrics (J_{VBVA}) and RMS(J_{VBPA}) while ensuring metrics RMS(J_{SDf}), RMS(J_{SDr}), RMS(J_{DTLf}),and RMS(J_{DTLr}) remain within acceptable bounds. Consequently, the objective function formulated to optimize IDES suspension system dynamic performance is expressed as Equation 36.

$$L = \rho_1 \frac{\mathrm{RMS}(J_{VBPA})}{\mathrm{RMS}(J_{VBPAO})} + \rho_2 \frac{\mathrm{RMS}(J_{VBVA})}{\mathrm{RMS}(J_{VBVAO})} \tag{36}$$

Vehicle dynamic performance must simultaneously consider ride comfort (vertical vibration) and handling stability (pitch vibration). In the formulation, weighting coefficients ρ_1 and ρ_2 for the body vertical acceleration and pitch angular acceleration are both set to 0.5, as they hold equal priority in the optimization objectives to prevent excessive optimization of a single metric from degrading other performance aspects. Metrics RMS(J_{VBVA}) and RMS(J_{VBPA}) represent the RMS values of the vertical and pitch angular accelerations of the vehicle body for the IDES suspension system, while metrics RMS(J_{VBVAO}) and RMS(J_{VBPAO}) denote those of the conventional suspension system.

During the parameter optimization process using genetic algorithms, for collision risk prevention, the RMS metrics of suspension dynamic deflections and wheel dynamic loads (at both vehicle ends) must be constrained within acceptable thresholds. Specifically, front/rear suspension deflection RMS must be capped at one-third of maximum travel, while dynamic wheel load RMS (front/rear) should not exceed one-third of static load RMS values. The corresponding constraint equations are as follows

$$\begin{cases} \mathrm{RMS}\left(J_{SDf}\right) \le S_{\max}/3 \\ \mathrm{RMS}\left(J_{SDr}\right) \le S_{\max}/3 \\ \mathrm{RMS}\left(J_{DTLf}\right) \le \left(m_{uf} + m_{sf}\right)\cdot g/3 \\ \mathrm{RMS}\left(J_{DTLr}\right) \le \left(m_{ur} + m_{sr}\right)\cdot g/3 \end{cases} \tag{37}$$

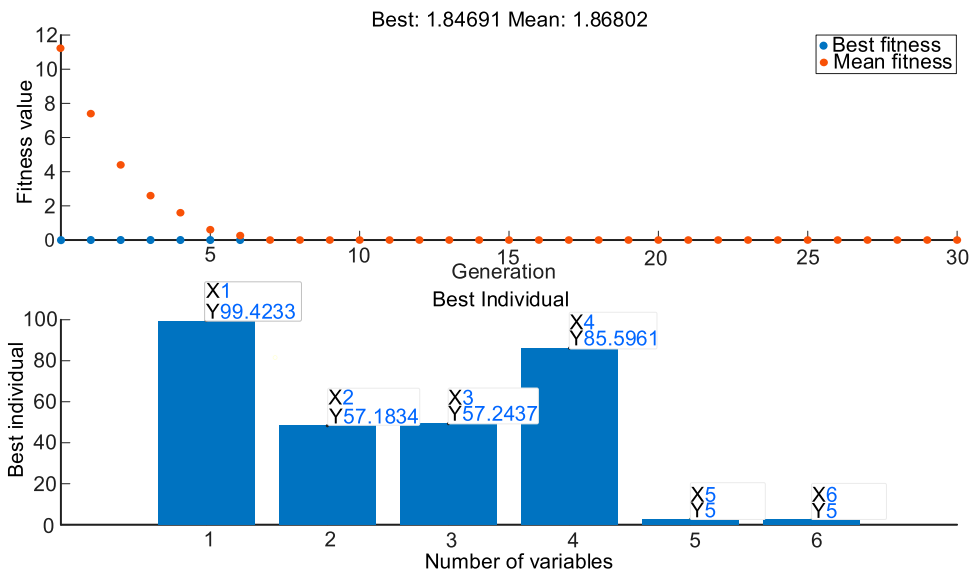

FIGURE 9
Genetic algorithm optimization process for IDES structural parameters.

TABLE 5 Optimized structural parameters of IDES suspension at different vehicle speeds. (Original parameters: $b_f = b_r = 200kg$, $c_{bf} = c_{br} = 1 \times 10^6 Ns/m^3$, $k_{bf} = k_{br} = 1 \times 10^3 N/m$).

Vehicle speed	5m/s	15m/s	35m/s
k_{bf} (N/m)	6.593×10^3	9.942×10^3	9.581×10^3
k_{br} (N/m)	8.618×10^3	5.718×10^3	5.533×10^3
c_{bf} (Ns/m^3)	7.763×10^6	5.724×10^6	7.607×10^6
c_{br} (Ns/m^3)	5.745×10^6	8.560×10^6	1.798×10^6
b_f (kg)	50	50	56.7
b_r (kg)	50	50	50

To ensure that the optimized parameters of the IDES suspension system align with the actual vehicle conditions, it is necessary to define the optimization range for the structural parameters.

$$\begin{cases} 2000N/m \le k_{bf} \le 3000N/m \\ 2000N/m \le k_{br} \le 3000N/m \\ 500Ns/m \le c_{bf} \le 2000Ns/m \\ 500Ns/m \le c_{br} \le 2000Ns/m \\ 0kg \le b_f \le 200kg \\ 0kg \le b_r \le 200kg \end{cases} \tag{38}$$

The parameter optimization process using a genetic algorithm is shown in Figure 8. Fundamentally, genetic algorithms emulate biological evolution's natural selection through operators like selection, crossover, and mutation, progressively generating individuals with enhanced environmental fitness. As a powerful and robust algorithm, the genetic algorithm effectively addresses the optimization problem of suspension system structural parameters. The specific optimization procedure is as follows:

1. Using MATLAB's built-in Genetic Algorithm Toolbox, the population size was set to 50, with 30 iterations performed. Selection, crossover, and mutation parameters were maintained at their default values. A real-number coding scheme was employed, with upper and lower bounds defined for each structural parameter. Under these settings, optimized parameters were efficiently obtained.
2. The genetic algorithm program and Simulink models of both suspension systems were integrated and executed. By aligning with the objective function and parameter constraints, the optimized structural parameters were determined once the termination criteria were satisfied.

Figure 9 shows the iteration steps of the genetic algorithm. The convergence curve stabilizes within 30 iterations, indicating that the algorithm has found a near-optimal solution. Minimal variation in the curve beyond 10–20 iterations confirms the rationality of algorithmic settings (e.g., population size of 50, default genetic operator parameters). Table 5 provides the optimized design parameters of the IDES mechanism at low (5 m/s), medium (15 m/s), and high speeds (35 m/s). These parameters were applied to IDES suspension system simulations to evaluate the dynamic performance of the genetically optimized mechanism. To visually demonstrate the superiority of the genetic algorithm, Figure 9 compares dynamic performance metrics (original suspension, unoptimized IDES, and optimized IDES systems) under low-, medium-, and high-speed conditions.

As illustrated in Figure 10, versus the original suspension system, the IDES suspension system optimized by genetic algorithm exhibits significantly consistent improvements in dynamic performance indicators across different vehicle speeds. Due to the physical coupling between vertical body acceleration and pitch angular acceleration, the latter exhibits a slight deterioration (still within the specified constraint limits), while all other five performance indicators show significant enhancement. To

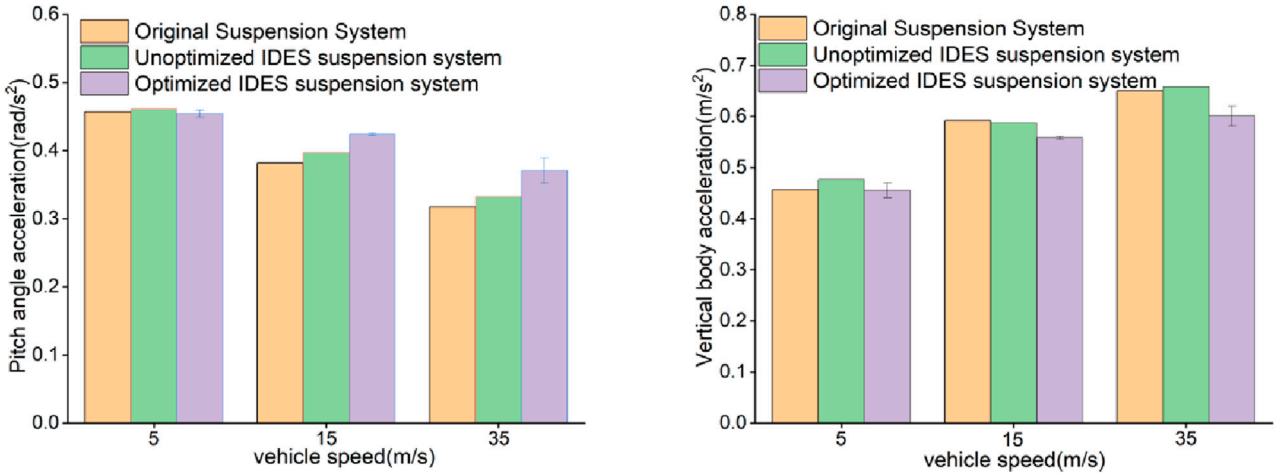

FIGURE 10
Comparison of dynamic performance indexes of three suspension systems at different speeds.

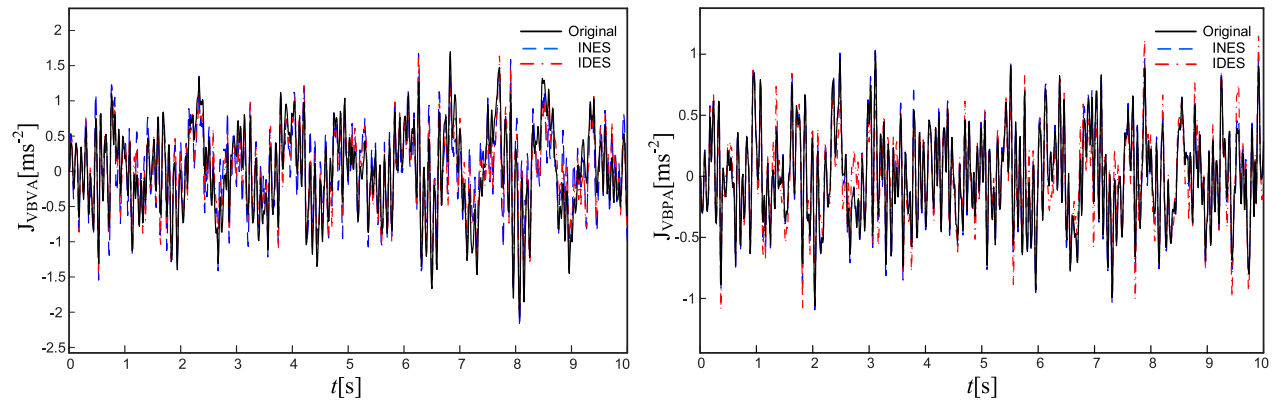

FIGURE 11
Compares the vertical body acceleration and pitch angular acceleration of the original half-car system, 518 and the optimized IDES and INES half-car systems under random excitation (v = 15 m/s).

further explore the specific effects of parameter optimization using genetic algorithms, this study selects medium vehicle speed as a typical operating condition for optimization analysis to obtain the most representative performance optimization results. A comparison is then made with the baseline suspension system and the optimized INES suspension system. The comparison of vertical body acceleration and pitch angular acceleration for the optimized IDES and INES suspension systems, as well as the baseline system, is shown in Figure 11, with specific dynamic performance indicators provided in Table 6.

As presented in Table 6, the optimized IDES suspension system achieves substantial reductions in the root-mean-square (RMS) values of body vertical acceleration, front and rear suspension dynamic deflections, and front and rear wheel dynamic loads by 5.56%, 9.20%, 15.56%, 11.37%, and 12.15%, respectively, in comparison with the original suspension system. Concurrently, the RMS value of body pitch angle acceleration remains at 0.4256 rad/s^2, which falls within the acceptable constraint range. These performance enhancements are preserved when the IDES system is compared to the optimized INES suspension system. Furthermore, as indicated by the analysis in Table 4, the IDES configuration delivers lower RMS values for front and rear suspension deflections and wheel dynamic forces relative to the unoptimized INES system, while sustaining similar levels of vertical acceleration and pitch angle acceleration performance.

Based on Tables 3–5, after optimization using the genetic algorithm, the inertial masses of the front and rear inerters are significantly reduced, which diminishes the amplification of high-frequency vibration energy and thereby improves the vehicle body vertical acceleration. The adjustment of the linear spring stiffness optimizes low-frequency energy transfer, resulting in improvements in certain wheel loads. The nonlinear damping coefficients are significantly increased, enhancing the energy dissipation under

TABLE 6 RMS values of dynamic performance indicators for optimized systems under stochastic road excitation (v = 15 m/s).

Dynamic performance metrics	Original	INES optimization	Percentage of vibration reduction	IDES optimization	Percentage of vibration reduction
$J_{VBVA}/(\mathrm{m}\cdot\mathrm{s}^{-2})$	0.5918	0.5821	1.63%	0.5589	5.56%
$J_{VBPA}/(\mathrm{rad}\cdot\mathrm{s}^{-2})$	0.3817	0.3668	3.90%	0.4256	−11.50%
$J_{SDf}/(\mathrm{m})$	0.0087	0.0086	1.15%	0.0079	9.20%
$J_{SDr}/(\mathrm{m})$	0.0090	0.0089	1.10%	0.0076	15.56%
$J_{DTLf}/(\mathrm{N})$	553.9300	559.2047	−0.95%	490.9308	11.37%
$J_{DTLr}/(\mathrm{N})$	555.4266	588.0702	−5.88%	487.9173	12.15%

high-energy conditions and further reducing suspension deflections and wheel loads.

However, the pitch angular acceleration is mainly determined by the force difference between the front and rear suspensions, while the vehicle body vertical acceleration represents the average vertical motion of the entire body. When the optimization algorithm focuses on reducing the overall vertical acceleration, it requires decreasing the inerter masses or increasing the front and rear damping to "suppress overall vibration." This can unbalance the front and rear suspension forces, leading to an increase in pitch angular acceleration in some configurations. Therefore, due to the optimization weighting favoring the overall vehicle body acceleration, pitch angular acceleration increases in certain cases, reflecting a trade-off between global ride comfort and local vibration indices.

Overall, the optimization results can be physically interpreted as achieving a comprehensive improvement in both body and suspension performance by reducing inertial mass, adjusting stiffness, and enhancing damping. The GA-optimized IDES suspension system achieves a comprehensive enhancement of vehicle dynamics through these combined adjustments.

6 Conclusion

This study applied the Inertially-Enhanced Damping Energy Sink (IDES) to a half-vehicle system to address the traditional Nonlinear Energy Sink (NES)'s reliance on nonlinear stiffness. A single-degree-of-freedom vibration model was first established to explore the optimal configuration of IDES. The effective IDES structure was then implemented in a half-vehicle model, and its dynamic response under harmonic road excitation was analyzed using the Harmonic Balance Method (HBM) and the Pseudo-Arc Length Method (PALM). Six performance indicators were used to evaluate the system's dynamic performance. Furthermore, the structural parameters of IDES were optimized using a genetic algorithm. The conclusions are summarized as follows:

1. Investigation into the optimal IDES configuration within the single-degree-of-freedom system revealed that the Series-Parallel Type I IDES suspension achieved the lowest resonance peak in suspension displacement under harmonic excitation, demonstrating the best vibration attenuation performance.
2. The half-vehicle model integrated with IDES constituted a nonlinear system, incorporating the nonlinear damping introduced by IDES. The analytical solutions derived via HBM and PALM showed strong agreement with numerical results, validating the effectiveness of these methods for solving such complex nonlinear systems.
3. Under both harmonic and random excitations, the IDES suspension system significantly reduced the resonance peaks of the system. However, the root-mean-square (RMS) value of the vehicle body's pitch angular acceleration experienced a slight increase.
4. After optimizing the IDES parameters with the genetic algorithm, the RMS values of the vertical body acceleration, suspension dynamic deflection, and tire dynamic load were significantly reduced, while the pitch angular acceleration was maintained within the designated constraint.

In summary, through the design of the Series-Parallel Type I IDES and parameter optimization via a genetic algorithm, this study enhanced the overall vibration suppression performance of the half-vehicle system while concurrently achieving a lightweight design. This work provides a viable new pathway for achieving wide-band vibration control and lightweight design in vehicle suspension systems. Future efforts will focus on manufacturing an IDES prototype and conducting experimental tests to validate the theoretical findings.

Data availability statement

The raw data supporting the conclusions of this article will be made available by the authors, without undue reservation.

Author contributions

YZ: Conceptualization, Formal Analysis, Writing – review and editing. RY: Data curation, Writing – original draft. WY: Validation, Writing – review and editing.

Funding

The authors declare that financial support was received for the research and/or publication of this article. The research described in this paper is supported by the Major Project of Basic Science (Natural Science) of the Jiangsu Higher Education Institutions (22KJA410001), the Changzhou Science and Technology Program (CZ20240019).

Conflict of interest

The authors declare that the research was conducted in the absence of any commercial or financial relationships that could be construed as a potential conflict of interest.

Generative AI statement

The authors declare that no Generative AI was used in the creation of this manuscript.

Any alternative text (alt text) provided alongside figures in this article has been generated by Frontiers with the support of artificial intelligence and reasonable efforts have been made to ensure accuracy, including review by the authors wherever possible. If you identify any issues, please contact us.

Publisher's note

Supplementary material

The Supplementary Material for this article can be found online at: https://www.frontiersin.org/articles/10.3389/fmech.2025.1729318/full#supplementary-material

References

Bi, F. R., Gou, X. G., Wu, H. J., and Xi, H. J. (2002). Influence analysis of nonlinear damping in shock absorbers on vehicle body vibration. *J. Vib. Eng.* 15 (2), 36–41. doi:10.16385/j.cnki.issn.1004-4523.2002.02.007

Chen, P., Yang, J. H., Lv, N., and Yang, X. D. (2025). A combined vibration isolation system with quasi-zero stiffness and bistable nonlinear energy sink. *J. Vib. Eng. Technol.* 13 (3), 219–234. doi:10.1007/s42417-025-01782-0

Du, H., and Zhang, N. (2008). Constrained H ∞ control of active suspension for a half-car model with a time delay in control. 222 (5), 665–684. doi:10.1243/09544070JAUTO299

Gendelman, O. V., Manevitch, L. I., Vakakis, A. F., and M'Closkey, R. (2001). Energy pumping in nonlinear mechanical oscillators: part I. Dynamics of the underlying Hamiltonian systems. *J. Appl. Mech.* 68 (1), 34–41. doi:10.1115/1.1345524

Hollari, R. N., Taghvaeipour, A., Aghdam, M. M., and González, F. (2014). "Novel co-simulation technique in the flexible analysis of a parallel robot[C]," in *2014 international conference on robotics and mechatronics (ICRoM)* (IEEE), 224–230. doi:10.1109/ICRoM57054.2022.10025339

Huang, W., Jiang, H., Huang, Y., and Wang, H. (2024). An Inerter-Enhanced bistable nonlinear energy sink for seismic response control of building structures. *J. Build. Eng.* 96, 110384. doi:10.1016/j.jobe.2024.110384

Javidialesaadi, A., and Wierschem, N. E. (2019). An Inerter-Enhanced nonlinear energy sink. *Mech. Syst. Signal Process.* 129, 449–454. doi:10.1016/j.ymssp.2019.04.047

Lamarque, C. H., Gendelman, O. V., Savadkoohi, A. T., and Etcheverria, E. (2011). Targeted energy transfer in mechanical systems by means of non-smooth nonlinear energy sink. *Acta Mech.* 221 (1-2), 175–200. doi:10.1007/s00707-011-0492-0

Li, H. Q. (2015). *Research on vibration suppression effectiveness of energy sink with nonlinear damping*. Harbin: Harbin Institute of Technology.

Liu, Q., Liu, H., and Zhang, J. (2025). Optimization of nonlinear energy sink using Euler-buckled beams combined with piezoelectric energy harvester. *Mech. Syst. Signal Process.* 223, 111812. doi:10.1016/j.ymssp.2024.111812

Lu, Z., and Chen, L. (2017). Some recent progresses in nonlinear passive isolations of vibrations. *Chin. J. Theor. Appl. Mech.* 49 (3), 550–564. doi:10.6052/0459-1879-17-064

Lu, Z., Yang, T., Brennan, M. J., Liu, Z., and Chen, L. (2017). Experimental investigation of a two-stage nonlinear vibration isolation system with high-static-low-dynamic stiffness. *J. Appl. Mech.* 84 (2), 021001. doi:10.1115/1.4034989

Lu, Z., Wang, Z. X., and Lu, X. L. (2020). A review on nonlinear energy sink technology. *J. Vib. Shock.* 39 (4), 1–16. doi:10.13465/j.cnki.jvs.2020.04.001

Philip, R., Santhosh, B., Balaram, B., and Awrejcewicz, J. (2023). Vibration control in fluid conveying pipes using NES with nonlinear damping. *Mech. Syst. Signal Process.* 192, 110250. doi:10.1016/j.ymssp.2023.110250

Rahikainen, J., González, F., Naya, M. N., Sopanen, J., and Mikkola, A. (2020). On the cosimulation of multibody systems and hydraulic dynamics. *Multibody Syst. Dyn.* 50 (2), 143–162. doi:10.1007/s11044-020-09727-z

Saeed, A. S., Al-Shudeifat, M. A., Vakakis, A. F., and Cantwell, W. J. (2020). Rotary-impact nonlinear energy sink for shock mitigation: analytical and numerical investigations. *Arch. Appl. Mech.* 90 (3), 495–521. doi:10.1007/s00419-019-01622-0

Smith, M. C. (2002). Synthesis of mechanical networks: the inerter. *IEEE Trans. Autom. Control* 47 (10), 1648–1662. doi:10.1109/TAC.2002.803532

Umair, M., and Hou, Z. (2024). Displacement and force transmissibility of a high-static-low-dynamic-stiffness isolator with geometric nonlinear damping. *J. Vib. Eng. Technol.* 12 (6), 7317–7324. doi:10.1007/s42417-023-01252-5

Vakakis, A. F. (2001). Inducing passive nonlinear energy sinks in vibrating systems. *J. Vib. Acoust.* 123 (3), 324–332. doi:10.1115/1.1368883

Wang, X., Ma, T. B., Ren, H. L., and Ning, J. G. (2014). A local pseudo arc-length method for hyperbolic conservation laws. *Acta Mech. Sin.* 30 (6), 956–965. doi:10.1007/s10409-014-0091-0

Wang, J., Zhang, C., and Zheng, Y. (2022). An Inerter-Enhanced asymmetric nonlinear energy sink for response mitigation of structures subjected to harmonic and seismic ground excitations. *Struct. Control Health Monit.* 29 (12), e3104. doi:10.1002/stc.3104

Wang, Y., Wang, P., Meng, H., and Chen, L. (2024a). Dynamic performance and parameter optimization of a half-vehicle system coupled with an Inerter-Based X-Structure nonlinear energy sink. *Appl. Math. Mech.* 45 (1), 85–110. doi:10.1007/s10483-024-3070-7

Wang, Y., Xu, B. B., Dai, J. G., and Chen, L. Q. (2024b). Enhanced dynamic performance of a half-vehicle system using Inerter-Based nonlinear energy sink. *J. Vib. Control* 30 (13-14), 2857–2880. doi:10.1177/10775463231186301

Wang, Y., Li, X., Wei, S., Wang, J., Ding, H., and Chen, L. (2025). Design and application of nonlinear energy sink in vibration control of a half-vehicle system. *Chin. J. Theor. Appl. Mech.* 57 (3), 720–729. doi:10.6052/0459-1879-24-537

Wu, W. L., and Tang, B. (2022). Analysis of a bio-inspired multistage nonlinear vibration isolator: an elliptic harmonic balance approach. *Arch. Appl. Mech.* 92 (1), 183–198. doi:10.1007/s00419-021-02049-2

Xiong, H., Kong, X. R., and Liu, Y. (2015). Influence of structural damping on a system with nonlinear energy sinks. *J. Vib. Shock* 34 (11), 116–121. doi:10.13465/j.cnki.jvs.2015.11.021

Zhang, Y. F., and Kong, X. R. (2023). Response analysis of vibration suppression in nonlinear energy sink with combined nonlinear damping. *Acta Mech. Sin.* 55 (4), 972–981. doi:10.6052/0459-1879-22-563

Zhang, Y. W., Lu, Y. N., Zhang, W., Teng, Y. Y., Yang, H. X., Yang, T. Z., et al. (2019). Nonlinear energy sink with inerter. *Mech. Syst. Signal Process.* 117, 52–64. doi:10.1016/j.ymssp.2018.08.026

Zhang, Y., Ren, C., Ma, K., Xu, Z., Zhou, P., and Chen, Y. (2022). Effect of delayed resonator on the vibration reduction performance of vehicle active seat suspension. *J. Low. Freq. Noise Vib. Act. Control* 41 (1), 387–404. doi:10.1177/14613484211046458

Zhang, Y. F., Kong, X. R., and Yue, C. F. (2023). Vibration analysis of a new nonlinear energy sink under impulsive load and harmonic excitation. *Commun. Nonlinear Sci. Numer. Simul.* 116, 106837. doi:10.1016/j.cnsns.2022.106837